

Spatial Polarization Multiplexing: Single-Shot Invisible Shape and Reflectance Recovery

Tomoki Ichikawa Ryo Kawahara Ko Nishino
Graduate School of Informatics, Kyoto University
<https://vision.ist.i.kyoto-u.ac.jp/research/spm/>

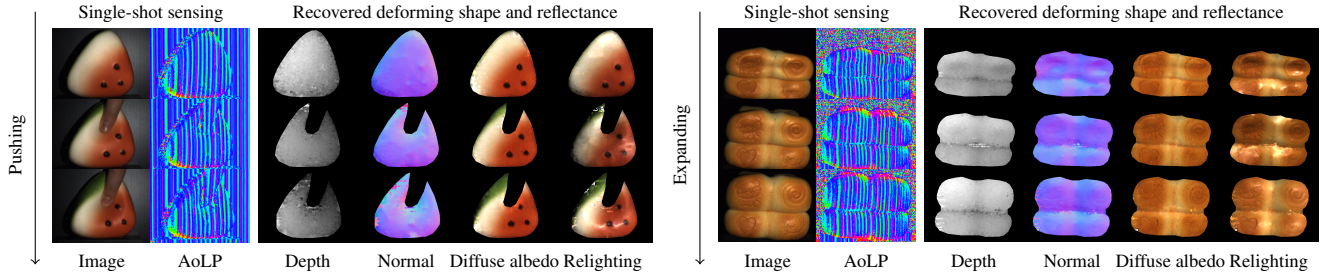


Figure 1. Spatial Polarization Multiplexing (SPM) recovers the shape and reflectance of a target in a single shot with a novel polarimetric structured light pattern that enables simultaneous decoding for shape reconstruction and decomposition of polarimetric diffuse and specular reflections. SPM enables these joint sensing per-frame of deforming objects without altering the appearance (invisible to the naked eyes). Left: a plush toy pushed down with a finger. Right: a soft loaf expanding after compression.

Abstract

We propose spatial polarization multiplexing (SPM) for joint sensing of shape and reflectance of a static or dynamic deformable object, which is also invisible to the naked eye. Past structured-light methods are limited to shape acquisition and cannot recover reflectance as they alter scene appearance. Our key idea is to spatially multiplex a polarization pattern to encode the incident ray and also densely sample the reflected light. We derive a quantized polarized light pattern that can be robustly and uniquely decoded from the reflected Angle of Linear Polarization (AoLP) values. It also enables single-shot disentanglement of polarimetric diffuse and specular reflections for accurate BRDF estimation. We achieve this spatial polarization multiplexing (SPM) with a constrained de Bruijn sequence. We validate this novel invisible single-shot shape and reflectance method with real static and dynamic objects. The results demonstrate the effectiveness of SPM for accurate shape and BRDF measurement which opens new avenues of application for 3D sensing thanks to its invisibility and ability to jointly recover the radiometric properties.

1. Introduction

The appearance of an object is dictated by its shape and reflectance. Recovering both from observations, *i.e.*, images, is essential for a multitude of applications including

real-world scene understanding, rendering, and virtual content creation. For this, inverse rendering has been widely studied in the computer vision field. Multi-view inverse rendering requires a calibrated multi-view capture setup, such as a capture dome [5, 9, 25, 33, 43, 57, 60]. Single-view inverse rendering is handy but challenging due to the ill-posedness caused by the entanglement of shape and reflectance, even when using additional cues like polarization. Learning-based single-view inverse rendering methods exploit learned priors to overcome this ill-posedness [4, 12, 31, 43, 59]. These methods, however, are fundamentally limited by the learned prior (*e.g.*, object types in training).

Structured light sensing does not suffer from these fundamental limitations as they directly measure the actual surface by encoding geometric and photometric cues into designed illuminations. A projector-camera system realizing structured light is easy to integrate into a single compact device. Single-shot structured light methods leverage a single spatial illumination (projector) pattern for shape acquisition. These methods cannot measure the reflectance as radiometric sensing inherently requires multiple observations under different lighting conditions [1, 24, 56]. The light pattern for shape sensing also alters the object appearance, making joint sensing of shape and reflectance challenging.

Can we design a structured light pattern that enables joint shape and reflectance sensing in a single shot? Such a single-shot shape and reflectance sensing can open new possibilities for 3D applications. Many natural and man-made

objects alter their shape and appearance as we interact with them. For instance, imagine picking up a loaf, a pillow, or a plush toy. Phase transitions and chemical reactions, *e.g.*, in baking or scientific experiments, also incur complex dynamics of the shape and appearance including swelling, shrinking, and material changes.

In this paper, we realize single-shot shape and reflectance sensing by fully leveraging polarization of light. We derive a novel single structured pattern with spatial polarization multiplexing, which we refer to as SPM, that enables robust decoding from its reflection by an object surface. Inspired by a recent polarization projector-camera system method (SPIDeRS) [24], SPM uses per-pixel Angle of Linear Polarization (AoLP) control for encoding and decoding polarization, instead of visible intensity or color. The method simultaneously encodes the incident ray and samples multiple polarimetric reflections. Since the polarization pattern is invisible to the naked eye, SPM can measure the shape and reflectance of the target without disrupting human experiences with them, *e.g.*, enable unnoticed sensing as people interact with their surroundings.

We design a stripe pattern with quantized AoLP so that their decoding after reflection can be achieved robustly and uniquely for shape and BRDF recovery. For this, we devise a de Bruijn sequence that is constrained to have different neighboring symbols and assign quantized AoLP values to these symbols. Adjacent stripes are designed to project different polarization states, which enables disentanglement of captured polarimetric image into polarimetric diffuse and specular reflections for single-shot reflectance recovery. Additional shifted patterns can be used to recover finer shape and reflectance when the object happens to be static. By continuously projecting these shifted patterns, the target can be measured at adaptive resolutions depending on the motion and deformation of the objects in the scene.

We validate the accuracy of structured polarization multiplexing on real data with quantitative and qualitative evaluation of measured shape and reflectance for complex static and deforming dynamic objects. We show the effectiveness of SPM for shape reconstruction, decomposition of polarimetric reflections, and relighting from a single shot as well as adaptive reconstruction of dynamic objects with opportunistic shifted SPM patterns. We believe our method establishes a novel foundation of instant spatio-temporal 3D and material capture and opens a new avenue of applications of real-world 3D sensing and appearance modeling.

2. Related Work

Table 1 compares our method with past single-view shape acquisition methods using active illumination.

Shape Sensing Structured light sensing measures 3D shape by decoding the reflected intensity or color patterns

Table 1. Unlike classic structured light, SPM only uses a single shot for recovering both the target geometry and radiometry and retains the natural object appearance as polarization is invisible to the naked eye.

Method	Single shot	BRDF acquisition	Invisible pattern
Single patt. SL	✓		
ToF	✓		✓
pToF [1]		✓	✓
Unified SL [56]		✓	
SPIDeRS [24]		✓	✓
Ours	✓	✓	✓

projected onto the target object. Several patterns have been proposed for different purposes [48]. Multi-pattern structured light [8, 18, 19, 39, 45, 50] enables robust and accurate shape measurement but is fundamentally limited to static scenes.

Single-pattern structured light [10, 27, 30, 42, 46, 47, 49] realizes shape reconstruction of dynamic scenes. Fourier transform profilometry methods estimate the height from a reference plane as the phase of a sinusoidal pattern [51, 53, 58]. Spatially multiplexed patterns use continuous intensity or wavelength gradation [7, 52] and discrete codes represented with different colors and geometric features [44, 61, 62]. Other methods avoid directly using correspondences for dynamic scene reconstruction [16, 38]. These methods, however, only focus on shape acquisition, and cannot recover the reflectance which is essential for analyzing, viewing, and editing the object appearance.

Joint Shape and Reflectance Sensing Several inverse rendering methods reconstruct shape and reflectance from multi-view images [5, 9, 25, 33, 43, 57, 60]. These multi-view methods, however, need multiple shots or cameras. Multiple shots prevent their application to dynamic scenes, and using multiple cameras requires a calibrated setup which can be cumbersome to realize. Although some methods address inverse rendering from only a single image [4, 12, 14, 31, 34, 35, 43, 59], they lack geometric constraints to reconstruct the 3D shape, *i.e.* depth, and have to heavily rely on learned priors. Learning-based methods are inherently limited by the training data, which is hard to come by, especially for joint shape and reflectance estimation, and are biased towards what the model has learned. Our interest is in actual sensing of the physical instance observed in the real world. That is, our goal is to achieve direct measurement of the physical surface both in geometry and radiometry, which can also serve as ground truth for any learning-based methods.

Controlled illumination helps disentangle shape and reflectance for accurate inverse rendering. A combination of multi-view capture and controlled illumination has been used to acquire shape and spatially varying reflectance [21, 22, 26, 41, 54, 63]. Single-view methods [2, 17, 37, 40]

reconstruct the surface normal and reflectance but cannot obtain depth. Recent works combine inverse rendering and active depth sensing, such as structured light and ToF, by using a dedicated projector-camera system [1, 56]. Ichikawa *et al.* [24] propose structured polarization for depth sensing with encoded AoLP patterns and also normal and reflectance recovery from polarimetric reflection. These methods, however, require multiple shots under different lighting conditions and are limited to a static scene.

In contrast, our method captures depth and reflectance in a single shot with a projector-camera system, which can directly be applied to dynamic scenes. Additionally, as the naked eye cannot perceive the polarization pattern, unlike structured light methods, our method retains the natural appearance of an object, which enables a wider range of applications (*e.g.*, 3D and appearance sensing without being noticed for robot and human object interactions for HCI, robotics, and UI).

3. Prerequisites

Let us first review key properties of polarized light [20]. For projection, we use the polarization projector introduced in [24, 32] which can control the angle of linear polarization orientation (AoLP) at each pixel. Please see the supplementary material for more details of its hardware implementation with a liquid crystal spatial light modulator.

Polarization Light is a transverse electromagnetic wave and the orientation of its oscillation plane varies over time. In contrast to unpolarized light which randomly changes its oscillating orientation, polarized light has a constant or periodically rotating oscillation plane. The former light is called linearly polarized and the latter is referred to as circularly polarized. Light can also be partially polarized, in-between polarized and unpolarized.

A polarization filter lets through only light with a specific oscillating orientation. Light intensity of partially polarized light after a polarization filter at angle ϕ_c becomes

$$I(\phi_c) = \bar{I}(1 + \rho_L \cos(2\phi_c - 2\phi_L)), \quad (1)$$

where \bar{I} is the average intensity over the filter angle, ρ_L is the Degree of Linear Polarization (DoLP), and ϕ_L is the Angle of Linear Polarization (AoLP). We can reconstruct a linear polarization state \bar{I} , ρ_L , and ϕ_L by capturing the light intensity passing through different filter angles. A polarimetric camera, *e.g.*, Lucid TRI050S-PC with polarization image sensor Sony IMX250MZR, has on-chip four polarization filters of different angles, 0° , 45° , 90° , and 135° , for each 2×2 matrix of the sensor array. It enables us to capture linear polarization states in a single shot. It cannot distinguish unpolarized and circularly polarized light.

Mueller calculus with Stokes vectors is a useful mathematical representation to formulate polarimetric behavior

on the surface. Stokes vector represents partially polarized light, defined as

$$\mathbf{s} = \begin{bmatrix} s_0 \\ s_1 \\ s_2 \\ s_3 \end{bmatrix} = \begin{bmatrix} I(0) + I(\frac{\pi}{2}) \\ I(0) - I(\frac{\pi}{2}) \\ I(\frac{\pi}{4}) - I(\frac{3}{4}\pi) \\ s_3 \end{bmatrix} = \begin{bmatrix} 2\bar{I} \\ 2\bar{I}\rho_L \cos(2\phi_L) \\ 2\bar{I}\rho_L \sin(2\phi_L) \\ s_3 \end{bmatrix}, \quad (2)$$

where s_0 represents the light intensity, s_1 and s_2 represent the linearly polarized light, and s_3 represents the circularly polarized light. From Eq. (2), the DoLP and AoLP can be recovered as

$$\rho_L = \frac{\sqrt{s_1^2 + s_2^2}}{s_0}, \quad \phi_L = \frac{1}{2} \tan^{-1} \left(\frac{s_2}{s_1} \right), \quad (3)$$

respectively. The Mueller matrix represents the change of the polarization state as

$$\mathbf{s}^o = \mathbf{M} \mathbf{s}^i, \quad (4)$$

where \mathbf{s}^i and \mathbf{s}^o are Stokes vectors of input and output light, respectively. We use Mueller calculus to analyze the polarimetric reflection on an object surface.

Polarimetric Reflection of Polarization Pattern The polarized light pattern emitted from the polarization projector gets reflected by the target object surface. A polarimetric reflectance model expresses the modulation of the polarization states by the surface with the Mueller matrix [2, 22, 23, 28]. Baek *et al.* [2] approximate the polarimetric specular and diffuse reflections, \mathbf{M}^s and \mathbf{M}^d , by assuming a co-axial setup

$$\mathbf{M} = \mathbf{M}^s + \mathbf{M}^d \approx c^s \begin{bmatrix} 1 & 0 & 0 & 0 \\ 0 & 1 & 0 & 0 \\ 0 & 0 & -1 & 0 \\ 0 & 0 & 0 & -1 \end{bmatrix} + c^d \begin{bmatrix} 1 & m_{01}^d & m_{02}^d & 0 \\ m_{10}^d & 0 & 0 & 0 \\ m_{20}^d & 0 & 0 & 0 \\ 0 & 0 & 0 & 0 \end{bmatrix}, \quad (5)$$

where c^s and c^d are radiometric specular and diffuse terms representing the shading and specular BRDFs, respectively, and m_{ij}^d consists of Fresnel transmittance on the surface.

SPIDeRS [24] analyzes these approximated polarimetric reflections for reflectance recovery from the reflected polarization pattern. This method, however, requires two additional uniform polarization patterns for robust decoding and BRDF reconstruction. In contrast, we design a novel polarization pattern by spatially multiplexing the AoLP and achieve joint recovery of shape and reflectance from purely a single polarimetric image capture.

4. Spatial Polarization Multiplexing

Many spatially-multiplexed structured light patterns have been proposed in the past [6, 44, 61] which are all used for

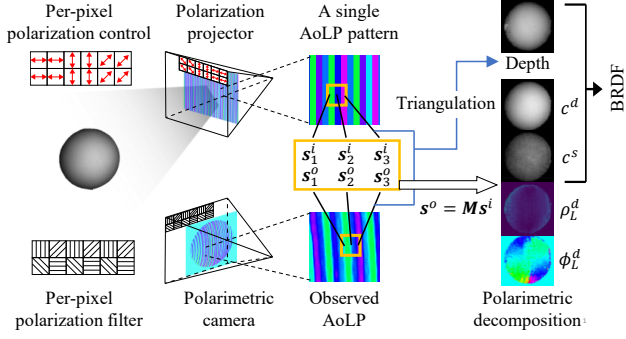


Figure 2. We design an SPM pattern with quantized stripes of AoLP values. Per-pixel polarization control enables robust decoding based on neighboring pixels and decomposition of captured polarimetric image into polarimetric diffuse and specular reflections for BRDF reconstruction.

intensity or color encoding and are also limited to shape acquisition. In sharp contrast, our focus is spatial multiplexing of polarized light for joint shape and reflectance acquisition.

For hardware configuration, we follow the projector-camera proposed in SPIDeRS [24]. To balance the co-axial assumption of polarimetric reflection for decoding and to ensure sufficient parallax, we locate the projector and camera with enough baseline at a distance from the target object. We also assume that there is no ambient light.

4.1. Quantization of AoLPs

Our method encodes and decodes structured polarization with AoLP values. As shown in Fig. 3, the diffuse reflection represented by $c^d m_{10}^d$ and $c^d m_{20}^d$ modulates the projected AoLP pattern. SPIDeRS [24] addressed this by capturing additional shots. To address this corruption in a single shot, the AoLP values used in SPM are quantized for robust decoding.

Let us show how quantization allows us to deal with the AoLP corruption by analyzing the effect of diffuse polarization represented as Eq. (5). We reparameterize m_{10}^d and m_{20}^d with the diffuse DoLP and AoLP

$$\rho_L^d = \sqrt{(m_{10}^d)^2 + (m_{20}^d)^2}, \quad \phi_L^d = \frac{1}{2} \tan^{-1} \left(\frac{m_{20}^d}{m_{10}^d} \right). \quad (6)$$

From Eqs. (4) to (6), the AoLP of the reflected light ϕ_L^o becomes

$$\phi_L^o = \frac{1}{2} \tan^{-1} \frac{c^d \rho_L^d \sin(2\phi_L^d) - c^s \rho_L^i \sin(2\phi_L^i)}{c^d \rho_L^d \cos(2\phi_L^d) + c^s \rho_L^i \cos(2\phi_L^i)}, \quad (7)$$

where ρ_L^i and ϕ_L^i are the DoLP and AoLP of the projected pattern, respectively. While the DoLP of the polarization projector ρ_L^i can be set to ≈ 1 [24], the DoLP of diffuse reflection is small. The diffuse DoLP ρ_L^d modeled as Fresnel transmission [2, 23] is much lower than 1.0 for all zenith

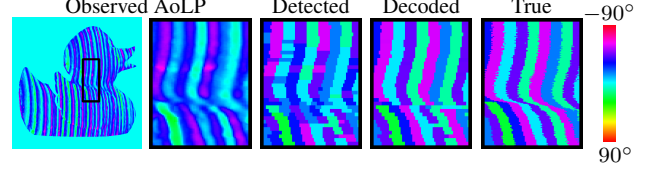


Figure 3. Pattern detection and decoding using quantized AoLP values. As shown in the inset, the observed AoLPs are corrupted due to diffuse reflection. “Detected”: the quantized AoLPs are incorrect where the corruption exceeds tolerance. “Decode”: our decoding corrects these mislabelings.

angles. In particular, when the refractive index is 1.5 and the zenith angle is less than 45° , the diffuse DoLP is $\rho_L^d < 0.05$.

We compute the AoLP modulation for $\frac{c^d}{c^s}$ when $\frac{\rho_L^d}{\rho_L^i} = 0.05$. When $\frac{c^d}{c^s} = 2$, $\frac{c^d}{c^s} = 3$, $\frac{c^d}{c^s} = 5$, the AoLP modulations are less than 2.9° , 4.3° , and 7.3° for all diffuse AoLP ϕ_L^d , respectively. Even when the diffuse reflection c^d is dominant, the AoLP change is within only a few degrees. In the supplementary material, we show the diffuse DoLP and AoLP modulation derivation in detail. When this AoLP corruption is smaller than the quantization width, the projected AoLP is correctly detected. Otherwise, decoding using dynamic programming [61] can correct mislabeling by leveraging the global pattern as described in Sec. 4.2.

Parallax also causes AoLP modulation by non-diagonal elements of polarimetric specular reflection in Eq. (5). When the angle between the viewing and lighting directions is less than 20° , AoLP change by Fresnel reflection is less than 1.2° [24]. As such, we can handle small parallax by AoLP quantization.

4.2. Spatial Polarization Multiplexing Pattern

We design an SPM pattern that enables simultaneous shape and BRDF recovery based on a de Bruijn sequence [44, 61] with quantized AoLP values. The substrings of length- n_{db} in a de Bruijn sequence are all unique, enabling unique decoding for shape reconstruction. An example is “012022110”. This sequence contains all nine substrings of $n_{db} = 2$ consisting of 0, 1, and 2, where 00 wraps around.

The polarization pattern is constructed by assigning the quantized AoLP values to the sequence symbols. As shown in Fig. 4, instead of directly using the de Bruijn sequence, two constraints are imposed on it. First, AoLP values of three sequential elements must be different for polarimetric diffuse and specular decomposition using neighboring pixels. Second, the differences between AoLP values of adjacent elements must be more than one quantization step for robust stripe detection. The constrained de Bruijn sequence can be constructed as an Eulerian path of a graph. In the supplementary material, we show how to modify an original graph by deleting the paths and nodes that violate our constraints.

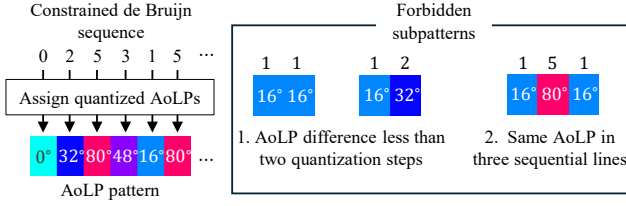


Figure 4. Example of our polarization pattern for $k_{db} = 6$, $n_{db} = 3$, and AoLP range $[0^\circ, 80^\circ]$. We impose constraints on the de Bruijn sequence to prevent adjacent stripes with identical or near AoLP values for polarimetric decomposition and robust detection of the pattern.

Reflected stripe pattern along each horizontal scanline in the captured polarimetric image is first detected. In the local window, each pixel votes for the symbols by quantizing the observed AoLP. The symbols that gather enough votes are selected and the center position of each is assigned the detected symbols. By sliding the local window, the symbols of the stripe pattern and their positions across the scanline can be detected.

Inspired by past structured scanline color decoding [44, 61], we use dynamic programming to decode the sequence of the detected symbols. The matching score is

$$\text{score}(d_i, p_j) = \cos(2\phi_{d_i} - 2\phi_{p_j}) - \cos(2\phi_{th}), \quad (8)$$

where ϕ_{d_i} and ϕ_{p_j} are the AoLP values corresponding to the symbols d_i and p_j at the i -th detected line and the j -th projected line, respectively. The threshold for matching is set as $\phi_{th} = 30^\circ$. Global matching using dynamic programming can handle mislabeling, misdetection, and occlusion.

The 3D points of decoded pixels can be reconstructed by triangulation—they are the intersection points of the camera ray and the plane projected as the stripe pattern. The decoding also provides a pair of incident and observed Stokes vectors for each point. Adjacent matched points on the scanline are used to separate polarimetric diffuse and specular reflections as described in Sec. 4.3.

4.3. Polarimetric Diffuse–Specular Decomposition

The decomposition of the Mueller matrix into polarimetric diffuse and specular reflections provides rich surface properties [2]. Measuring the Mueller matrix, however, requires multiple polarimetric images while rotating the polarization orientation of incident light.

As shown in Fig. 2, neighboring projector pixels of SPM with different polarization states can be used for single shot separation of polarimetric diffuse and specular reflections. Although diffuse polarization is ignored during AoLP quantization for robust decoding, it can be reconstructed by directly using the observed Stokes vectors of each correspondence.

For robust polarimetric decomposition, the Mueller matrix elements from Eq. (5) can be reduced by exploiting the near co-axial projector-camera setting as

$$\begin{aligned} m_{12} = m_{21} = 0, \quad m_{33} = m_{22} = -m_{11}, \\ m_{30} = m_{31} = m_{32} = m_{03} = m_{13} = m_{23} = 0, \end{aligned} \quad (9)$$

where m_{ij} is the (i, j) element of the Mueller matrix M of the target surface. A transpositional reciprocity relationship of the Mueller matrix [13] can also be leveraged, where the interchanging of incident light and viewing directions results in transposition

$$m_{10} = m_{01}, \quad m_{20} = -m_{02}. \quad (10)$$

From Eqs. (9) and (10), the Mueller matrix has four remaining elements: m_{00} , m_{11} , m_{10} , and m_{20} . Since the Stokes vector of linear polarization has three elements, at least two pairs of projected and observed Stokes vectors are required. This indicates that our SPM is essential to reconstruct these Mueller matrix elements.

By using the pairs of observed and incident Stokes vectors at the matched point and its adjacent matched points, m_{00} , m_{10} , m_{20} and m_{11} are reconstructed. First, the second and third rows of the Mueller matrix are computed as

$$\begin{bmatrix} s_{1,1}^o \\ s_{1,2}^o \\ \vdots \\ s_{N,1}^o \\ s_{N,2}^o \end{bmatrix} = \begin{bmatrix} s_{1,0}^i & 0 & s_{1,1}^i \\ 0 & s_{1,0}^i & -s_{1,2}^i \\ \vdots & \vdots & \vdots \\ s_{N,0}^i & 0 & s_{N,1}^i \\ 0 & s_{N,0}^i & -s_{N,2}^i \end{bmatrix} \begin{bmatrix} m_{10} \\ m_{20} \\ m_{11} \end{bmatrix}, \quad (11)$$

where $s_{k,j}^{i/o}$ is the j -th element of the k -th observed Stokes vector $s_k^{i/o}$ and N is the number of used Stokes vector pairs. Then, m_{00} is computed from a single Stokes vector pair for each correspondence as

$$m_{00} = \frac{s_0^o - s_1^i m_{10} + s_2^i m_{20}}{s_0^i}. \quad (12)$$

Polarimetric diffuse and specular reflections are then extracted:

$$\begin{aligned} c^s = m_{11}, \quad c^d = m_{00} - m_{11}, \\ m_{10}^d = m_{01}^d = \frac{m_{10}}{c^d}, \quad m_{20}^d = -m_{02}^d = \frac{m_{20}}{c^d}. \end{aligned} \quad (13)$$

4.4. BRDF Estimation

SPM enables BRDF recovery using the measured 3D shape and decomposed polarimetric reflections of the target. We adopt the Fresnel microfacet BRDF model [23], which describes polarimetric and radiometric surface (specular) and body (diffuse) reflections in a unified model. Initial surface normals of the reconstructed point cloud can be computed

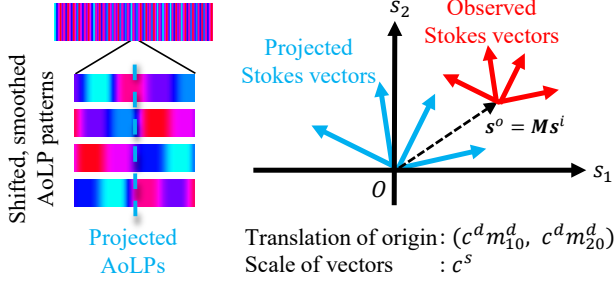


Figure 5. We smooth and shift the SPM pattern for high-resolution reconstruction of a static scene. We also change the AoLP assignment for each pattern to ensure sufficient variations of projected polarization states. The projected Stokes vectors are scaled and translated. The matching between the observed and projected Stokes vectors provides pixel-wise correspondences.

with Principal Component Analysis (PCA) of neighboring points.

We assume that the material parameters, refractive index μ , surface reflection albedo k_s , and microfacet distribution α and β , are uniform on the surface. For body reflection, we assume mesoscopic roughness κ is fixed at 0 and body reflection albedo \mathbf{K}_b is spatially varying. First, the surface normals and material parameters are estimated from the specular reflection and the diffuse polarization as

$$\arg \min_{\substack{\mu, k_s, \alpha, \\ \beta, \mathbf{N}}} \sum_i^L |c_i^s - \bar{c}_i^s|^2 + \lambda_d |m_{i,10}^d - \bar{m}_{i,10}^d|^2 + \lambda_d |m_{i,20}^d - \bar{m}_{i,20}^d|^2 + \lambda_n \|\mathbf{n}_i - \mathbf{n}_i^{\text{init}}\|, \quad (14)$$

where \bar{c}_i^s is the rendered component at the i -th correspondence, L is the number of correspondences, \mathbf{N} is a collection of surface normals \mathbf{n}_i , and $\mathbf{n}_i^{\text{init}}$ is the initial normals. We set $\lambda_d = 0.01$ and $\lambda_n = 0.001$. Then, the diffuse reflection albedo values are recovered as

$$\arg \min_{\mathbf{K}_b} \sum_i^L |c_i^d - \bar{c}_i^d|^2. \quad (15)$$

Since the body reflection albedo $k_{b,i} \in \mathbf{K}_b$ represents the scale of \bar{c}_i^d , Eq. (15) admits an analytical solution.

5. Shifted Spatial Polarization Multiplexing

The resolution of the sensed surface is limited by the stripe width of the SPM pattern. For a static scene, multiple shifted SPM patterns can be leveraged for high-resolution reconstruction. Furthermore, by continuously projecting the shifted patterns, the reconstruction resolution can be adapted to the scene—higher resolution for static regions and lower resolution for dynamic regions.

5.1. High-Resolution Recovery for Static Scene

As shown in Fig. 5, to obtain dense, sub-pixel correspondences, we smooth the edge of the SPM pattern by applying a Gaussian filter. For matching between smoothed patterns and polarimetric images, we directly use Stokes vectors, instead of the non-linearly modulated reflected AoLPs.

The Stokes vectors are linearly transformed by the Mueller matrix, as represented with Eqs. (4) and (5). The observed Stokes vectors of linear polarization become

$$s_1^o = c^d m_{10}^d + c^s s_1^i, \quad s_2^o = c^d m_{20}^d - c^s s_2^i. \quad (16)$$

Equation (16) indicates s_1^o and s_2^o are scaled by c^s and translated by $c^d m_{10}^d$ and $c^d m_{20}^d$.

When multiple polarimetric images are available, pixel-wise correspondences can be established by defining the matching cost to simultaneously estimate the scale and translation. While correct matching yields small residuals between the observed and incident Stokes vectors with the optimal scale and translation, incorrect matching yields larger residuals. The matching cost function reflects this with

$$C(\mathbf{S}_k^o, \mathbf{S}_j^i) = \min_{a, b_1, b_2} \|a \mathbf{S}_j^i + b_1 \mathbf{1}_o + b_2 \mathbf{1}_e - \mathbf{S}_k^o\|^2 + \min_{a, b_1, b_2} \|a \mathbf{S}_k^o + b_1 \mathbf{1}_o + b_2 \mathbf{1}_e - \mathbf{S}_j^i\|^2, \quad (17)$$

where \mathbf{S}_k^o and \mathbf{S}_j^i are the stacks of observed and projected Stokes vectors of the k -th and the j -th pixels on the scanline, respectively, $\mathbf{1}_o$ are vectors whose odd-numbered elements are 1 and else 0, and $\mathbf{1}_e$ are vectors whose even-numbered elements are 1 and else 0. Note that the signs of s_2^i in \mathbf{S}_j^i are inverted. The symmetric cost function stabilizes matching even when the norm of \mathbf{S}_k^o is close to zero [61].

Following [61], by inverting the matching cost, the matching score function is defined as

$$\text{score}(\mathbf{S}_k^o, \mathbf{S}_j^i) = C_0 - C(\mathbf{S}_k^o, \mathbf{S}_j^i), \quad (18)$$

where the matching threshold C_0 is

$$C_0 = (1 - t) \min_{k,j} C(\mathbf{S}_k^o, \mathbf{S}_j^i) + t \max_{k,j} C(\mathbf{S}_k^o, \mathbf{S}_j^i), \quad (19)$$

with $t = 0.2$. Sub-pixel correspondences is computed by refining the pixel-wise correspondences with local maxima of the score function with respect to projector pixels. We fit the parabola to the points $(j - 1, \text{score}(\mathbf{S}_k^o, \mathbf{S}_{j-1}^i))$, $(j, \text{score}(\mathbf{S}_k^o, \mathbf{S}_j^i))$, and $(j + 1, \text{score}(\mathbf{S}_k^o, \mathbf{S}_{j+1}^i))$, and obtain its peak as the sub-pixel correspondences.

After establishing the correspondences, multiple pairs of the projected and observed Stokes vectors are obtained for each pixel. From Eqs. (11) to (15), polarimetric diffuse and specular reflections are extracted and then the BRDF is recovered. To ensure sufficient variations of projected polarization states for the polarimetric reflectance decomposition, the AoLP assignment for each shifted pattern is changed.

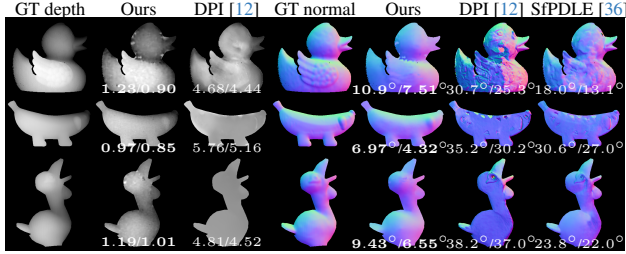


Figure 6. Shape reconstruction results of real-world objects and comparisons with learning-based methods using polarization. The numbers show the mean and median of depth errors in millimeters and surface normal angular errors in degrees. Our method robustly reconstructs shapes regardless of surface textures and materials in a single shot.

5.2. Adaptive Resolution for Dynamic Scene

When capturing the continuously shifted spatial polarization multiplexing, the target surface may be static for some regions or frames and dynamic for others. To fully leverage our shifted patterns even in dynamic scenes, we adapt the number of polarimetric images used for reconstruction, depending on whether each region is dynamic or static.

As shown in Fig. 10, each pixel in frame is labeled as “dynamic” or “static.” Since the polarization pattern has little effect on the object appearance, the differences in light intensity s_0^o between frames can be used for this labeling. When the intensity does not change between frames, the pixel is static. Otherwise, the pixel is dynamic. We use each polarimetric image at the dynamic pixels and multiple polarimetric images of continuous frames at the static pixels for decoding and reconstruction. To obtain the correspondences by dynamic programming, the detected stripe of the dynamic regions and all pixels of the static regions are concatenated to compute the matching score by switching the score functions.

6. Experimental Results

We experimentally validate the effectiveness of our method on real data. Our polarization projector consists of a white LED telecentric illuminator with a polarizer, a spatial light modulator with a resolution of 1024×768 (HOLOEYE LC2012), and convex lenses. We capture polarimetric images with a commercial RGB polarimetric camera (Lucid TRI050S-QC).

For RGB reconstruction, the green channel is used for shape reconstruction and the Mueller matrix elements in Eqs. (11) and (12) are computed for each channel. All color channels are used in Eq. (14) to optimize color-independent material parameters. Diffuse albedo is obtained from Eq. (15) for each color channel.

Line widths of the stripe patterns are set to 12 pixels on the polarization projector for the single pattern and 12 shifted patterns. We set $n_{db} = 4$ and $k_{db} = 7$, and quantize

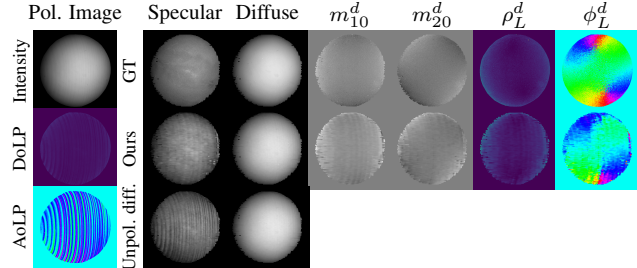


Figure 7. Decomposition results of a polarimetric reflection. Assuming unpolarized diffuse reflection causes artifacts in the separated specular component. In contrast, our method accurately decomposes polarimetric reflection in a single shot.

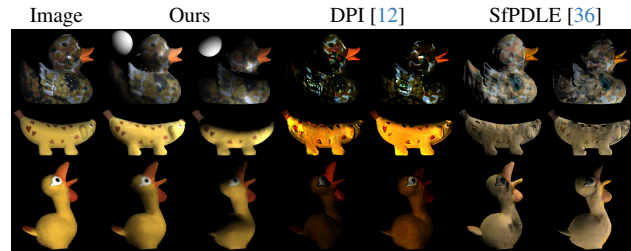


Figure 8. Relighting results using shape and BRDF. The Lambertian sphere indicates the direction of light. We can relight real-world objects in a single shot by fully exploiting polarimetric reflections of the SPM pattern.

the AoLP values at even intervals from 0° to 80° . For dense visualization of the results, the depths and the optimized BRDF parameters of the sparse single-shot reconstruction are interpolated by a radial basis function.

6.1. Shape Reconstruction

Figure 6 shows shape reconstruction results on real objects. We obtain the ground truth shapes by structured light with Gray code and phase-shifting patterns. The numbers below each depth map show the mean and median of depth errors and those below each normal map show the angular errors. The results show that our method can measure accurate object geometry robustly from the single SPM pattern.

6.2. Polarimetric Decomposition

Figure 7 shows the results of the polarimetric specular and diffuse decomposition. We compute the ground truth decomposition results from the ground truth Mueller matrix, following Eq. (13). The ground truth Mueller matrix is obtained from 26 polarimetric images while projecting different uniform polarization patterns, and by solving Eq. (4). Unpolarized diffuse reflection is often assumed for single-shot diffuse and specular separation [55]. This assumption, however, leads to inaccurate specular reflection as diffuse reflection is, in reality, partially polarized. In contrast, our method can successfully decompose a single polarimetric

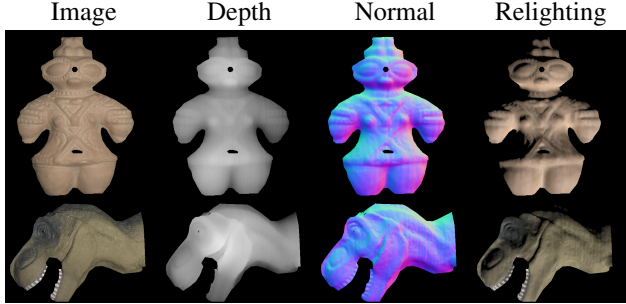


Figure 9. High-resolution reconstruction of static scenes by using shifted SPM patterns. The shifted SPM enables shape and reflectance sensing of detailed surface texture.

image into polarimetric diffuse and specular reflections by exploiting the spatially multiplexed polarization.

6.3. Relighting

Figure 8 shows relighting results by using the reconstructed shape and BRDF. Polarimetric specular and diffuse decomposition enables BRDF estimation from a single polarimetric image. The relighting results show plausible surface color texture and specular highlight rendering under novel lighting conditions. Note again that past single-shot sensing methods alter the visual texture and thus cannot achieve this from the single capture.

6.4. Comparison with Learning-based Methods

We compare our method with learning-based methods that use single RGB polarimetric images. Deep Polarization Imaging [12] (DPI) and Shape from Polarization with Distant Lighting Estimation [36] (SfPDLE) estimate a normal map and SVBRDF. DPI also estimates a depth map. We align the domain of illumination with their training data. Figures 6 and 8 shows the shape reconstructions and the RGB relighting results. The scale of the depth map of DPI is adjusted for comparison. Learning-based methods suffer from heavy reliance on learned priors which manifests into strong biases appearing as distortions of the recovered shape. Our SPM method realizes actual sensing of accurate shape and reflectance of the actual shape without any reliance on pre-learned priors, which is critical for real-world unseen targets.

6.5. Dynamic Surface Reconstruction

We apply our method to a dynamic surface by capturing continuous frames and using each frame. Figure 1 shows the shape reconstruction and relighting results of a pushed squeeze toy and a fake loaf expanding after compression. Our method can capture changes in both shape and reflectance and relight the dynamic deformable surface at each frame.

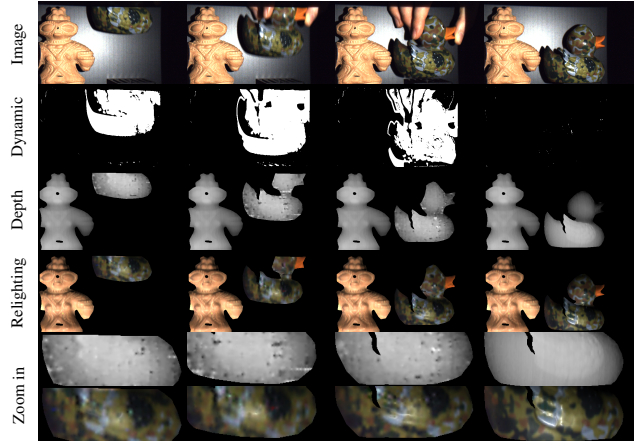


Figure 10. Adaptive resolution reconstruction of a scene with both dynamic and static frames by using shifted SPM patterns. A static clay figure is reconstructed in high resolution. A camouflage-printed rubber duck is reconstructed in low resolution when moving and in high resolution after stopping.

6.6. Adaptive High Resolution Sensing

Figure 9 shows high-resolution reconstruction results of a static scene. Our method for shifted patterns can capture the detailed shape and texture at the resolution of the polarimetric camera. Figure 10 demonstrates the adaptive resolution reconstruction of a dynamic scene. Our method simultaneously reconstructs both dynamic and static regions at adaptive resolutions for each region and frame.

7. Conclusion

We introduced a novel method for direct, single-shot, simultaneous sensing of shape and reflectance that is invisible to the naked eye. This is achieved by introducing spatial polarimetric multiplexing with quantized AoLPs and a constrained de Bruijn sequence and decoding of it for polarimetric reflectance separation and BRDF recovery. We further showed that shifted SPM patterns can be leveraged for adaptive and high-resolution reconstruction of dynamic and static scenes, regardless of surface texture and materials. We believe our spatial polarization multiplexing opens a new avenue of applications of single-shot shape and reflectance sensing thanks to its robustness to color, texture, and materials, applicability to both static and dynamic surfaces, and invisibility to human eyes. We are hopeful that it will find use in medicine (*e.g.*, real-time surgery assistance), VR/AR (*e.g.*, human-object interaction), robotics (especially for human-robot collaboration), and, of course, computer vision. One limitation we plan to overcome in our immediate future work is the requirement of absence of environmental light. We show that our SPM can provide some cues under environmental light in the supplementary material. Achieving the same in broad daylight will further expand the horizon of applications.

Acknowledgement This work was in part supported by JSPS KAKENHI 21H04893, 23K28110, 24H00742, 23KJ1367; and JST JPMJAP2305.

References

- [1] Seung-Hwan Baek and Felix Heide. All-photon Polarimetric Time-of-Flight Imaging. In *CVPR*, pages 17876–17885, 2022. 1, 2, 3
- [2] Seung-Hwan Baek, Daniel S. Jeon, Xin Tong, and Min H. Kim. Simultaneous Acquisition of Polarimetric SVBRDF and Normals. *ACM TOG*, 37:1 – 15, 2018. 2, 3, 4, 5
- [3] Seung-Hwan Baek, Tizian Zeltner, Hyunjin Ku, Inseung Hwang, Xin Tong, Wenzel Jakob, and Min H Kim. Image-Based Acquisition and Modeling of Polarimetric Reflectance. *ACM TOG*, 39(4):139, 2020. 4
- [4] Jonathan T Barron and Jitendra Malik. Shape, Illumination, and Reflectance from Shading. *IEEE TPAMI*, 37(8):1670–1687, 2014. 1, 2
- [5] Sai Bi, Zexiang Xu, Kalyan Sunkavalli, David Kriegman, and Ravi Ramamoorthi. Deep 3D Capture: Geometry and Reflectance from Sparse Multi-View Images. In *CVPR*, pages 5960–5969, 2020. 1, 2
- [6] Kim L Boyer and Avinash C Kak. Color-encoded Structured Light for Rapid Active Ranging. *IEEE TPAMI*, PAMI-9(1): 14–28, 1987. 3
- [7] Brian Carrhill and Robert Hummel. Experiments with the Intensity Ratio Depth Sensor. *Computer Vision, Graphics, and Image Processing*, 32(3):337–358, 1985. 2
- [8] Dalit Caspi, Nahum Kiryati, and Joseph Shamir. Range Imaging with Adaptive Color Structured Light. *IEEE TPAMI*, 20(5):470–480, 1998. 2
- [9] Ziang Cheng, Hongdong Li, Yuta Asano, Yinqiang Zheng, and Imari Sato. Multi-View 3D Reconstruction of a Textureless Smooth Surface of Unknown Generic Reflectance. In *CVPR*, pages 16226–16235, 2021. 1, 2
- [10] Pengyu Cong, Zhiwei Xiong, Yueyi Zhang, Shenghui Zhao, and Feng Wu. Accurate Dynamic 3D Sensing with Fourier-assisted Phase Shifting. *IEEE Journal of Selected Topics in Signal Processing*, 9(3):396–408, 2014. 2
- [11] Robert L Cook and Kenneth E. Torrance. A Reflectance Model for Computer Graphics. *ACM TOG*, 1(1):7–24, 1982. 4
- [12] Valentin Deschaintre, Yiming Lin, and Abhijeet Ghosh. Deep Polarization Imaging for 3D Shape and SVBRDF Acquisition. In *CVPR*, pages 15567–15576, 2021. 1, 2, 7, 8, 3
- [13] Yuqi Ding, Yu Ji, Zhang Chen, Mingyuan Zhou, Sing Bing Kang, and Jinwei Ye. Polarimetric Helmholtz Stereopsis. *IEEE TPAMI*, 46(07):4597–4611, 2024. 5
- [14] Yuto Enyo and Ko Nishino. Diffusion Reflectance Map: Single-Image Stochastic Inverse Rendering of Illumination and Reflectance. In *CVPR*, pages 11873–11883, 2024. 2
- [15] Harold Fredricksen. A Survey of Full Length Nonlinear Shift Register Cycle Algorithms. *SIAM review*, 24(2):195–221, 1982. 1
- [16] Ryo Furukawa, Ryusuke Sagawa, and Hiroshi Kawasaki. Depth Estimation Using Structured Light Flow—Analysis of Projected Pattern Flow on an Object’s Surface. In *ICCV*, pages 4640–4648, 2017. 2
- [17] Abhijeet Ghosh, Tongbo Chen, Pieter Peers, Cyrus A Wilson, and Paul Debevec. Circularly Polarized Spherical Illumination Reflectometry. *ACM TOG*, 29(6):1–12, 2010. 2
- [18] Mohit Gupta and Nikhil Nakhate. A Geometric Perspective on Structured Light Coding. In *ECCV*, pages 87–102, 2018. 2
- [19] Mohit Gupta and Shree K Nayar. Micro Phase Shifting. In *CVPR*, pages 813–820. IEEE, 2012. 2
- [20] Eugene Hecht. *Optics*. Pearson, 5 edition, 2016. 3
- [21] Michael Holroyd, Jason Lawrence, and Todd Zickler. A Coaxial Optical Scanner for Synchronous Acquisition of 3D Geometry and Surface Reflectance. *ACM TOG*, 29(4):1–12, 2010. 2
- [22] Inseung Hwang, Daniel S Jeon, Adolfo Muñoz, Diego Gutierrez, Xin Tong, and Min H Kim. Sparse Ellipsometry: Portable Acquisition of Polarimetric SVBRDF and Shape with Unstructured Flash Photography. *ACM TOG*, 41(4):1–14, 2022. 2, 3
- [23] Tomoki Ichikawa, Yoshiki Fukao, Shohei Nobuhara, and Ko Nishino. Fresnel Microfacet BRDF: Unification of Polarimetric Surface-Body Reflection. In *CVPR*, pages 16489–16497, 2023. 3, 4, 5, 2
- [24] Tomoki Ichikawa, Shohei Nobuhara, and Ko Nishino. SPI-DeRS: Structured Polarization for Invisible Depth and Reflectance Sensing. In *CVPR*, pages 25077–25085, 2024. 1, 2, 3, 4
- [25] Yingwenqi Jiang, Jiadong Tu, Yuan Liu, Xifeng Gao, Xiaoxiao Long, Wenping Wang, and Yuexin Ma. GaussianShader: 3D Gaussian Splatting with Shading Functions for Reflective Surfaces. In *CVPR*, pages 5322–5332, 2024. 1, 2
- [26] Kaizhang Kang, Cihui Xie, Chengan He, Mingqi Yi, Minyi Gu, Zimin Chen, Kun Zhou, and Hongzhi Wu. Learning Efficient Illumination Multiplexing for Joint Capture of Reflectance and Shape. *ACM TOG*, 38(6):165–1, 2019. 2
- [27] Hiroshi Kawasaki, Ryo Furukawa, Ryusuke Sagawa, and Yasushi Yagi. Dynamic Scene Shape Reconstruction Using a Single Structured Light Pattern. In *CVPR*, pages 1–8. Ieee, 2008. 2
- [28] Yuhi Kondo, Taishi Ono, Legong Sun, Yasutaka Hirasawa, and Jun Murayama. Accurate Polarimetric BRDF for Real Polarization Scene Rendering. In *ECCV*, pages 220–236. Springer, 2020. 3
- [29] Chenhao Li, Taishi Ono, Takeshi Uemori, Sho Nitta, Hajime Mihara, Alexander Gatto, Hajime Nagahara, and Yusuke Moriuchi. NeISF++: Neural Incident Stokes Field for Polarized Inverse Rendering of Conductors and Dielectrics. In *CVPR*, pages 26493–26503, 2025. 4
- [30] Yue Li, Jiayong Peng, Yueyi Zhang, and Zhiwei Xiong. Self-Distilled Depth From Single-Shot Structured Light With Intensity Reconstruction. *IEEE Transactions on Computational Imaging*, 9:678–691, 2023. 2
- [31] Zhengqin Li, Zexiang Xu, Ravi Ramamoorthi, Kalyan Sunkavalli, and Manmohan Chandraker. Learning to recon-

- struct shape and spatially-varying reflectance from a single image. *ACM TOG*, 37(6):1–11, 2018. 1, 2
- [32] Zhuoxiao Li, Zhihang Zhong, Shohei Nobuhara, Ko Nishino, and Yinqiang Zheng. Fooling Polarization-based Vision using Locally Controllable Polarizing Projection. In *CVPR*, pages 24706–24715, 2024. 3, 1
- [33] Zhihao Liang, Qi Zhang, Ping Feng, Ying Shan, and Kui Jia. GS-IR: 3D Gaussian Splatting for Inverse Rendering. In *CVPR*, pages 21644–21653, 2024. 1, 2
- [34] Stephen Lombardi and Ko Nishino. Single Image Multimaterial Estimation. In *CVPR*, pages 238–245. IEEE, 2012. 2
- [35] Stephen Lombardi and Ko Nishino. Reflectance and Illumination Recovery in the Wild. *IEEE TPAMI*, 38(1):129–141, 2015. 2
- [36] Youwei Lyu, Lingran Zhao, Si Li, and Boxin Shi. Shape from Polarization with Distant Lighting Estimation. *IEEE TPAMI*, 45(11):13991–14004, 2023. 7, 8, 2, 3
- [37] Wan-Chun Ma, Tim Hawkins, Pieter Peers, Charles-Felix Chabert, Malte Weiss, and Paul E Debevec. Rapid Acquisition of Specular and Diffuse Normal Maps from Polarized Spherical Gradient Illumination. In *Proceedings of the 18th Eurographics Conference on Rendering Techniques*, pages 183–194, 2007. 2
- [38] Parsa Mirdehghan, Maxx Wu, Wenzheng Chen, David B Lindell, and Kiriakos N Kutulakos. TurboSL: Dense Accurate and Fast 3D by Neural Inverse Structured Light. In *CVPR*, pages 25067–25076, 2024. 2
- [39] Daniel Moreno, Kilho Son, and Gabriel Taubin. Embedded Phase Shifting: Robust Phase Shifting with Embedded Signals. In *CVPR*, pages 2301–2309, 2015. 2
- [40] Giljoo Nam, Joo Ho Lee, Hongzhi Wu, Diego Gutierrez, and Min H Kim. Simultaneous Acquisition of Microscale Reflectance and Normals. *ACM TOG*, 35(6):185–1, 2016. 2
- [41] Giljoo Nam, Joo Ho Lee, Diego Gutierrez, and Min H Kim. Practical SVBRDF Acquisition of 3D Objects with Unstructured Flash Photography. *ACM TOG*, 37(6):1–12, 2018. 2
- [42] Andrew-Hieu Nguyen, Brian Sun, Charlotte Qiong Li, and Zhaoyang Wang. Different structured-light patterns in single-shot 2D-to-3D image conversion using deep learning. *Applied Optics*, 61(34):10105–10115, 2022. 2
- [43] Geoffrey Oxholm and Ko Nishino. Shape and Reflectance Estimation in the Wild. *IEEE TPAMI*, 38(2):376–389, 2015. 1, 2
- [44] Jordi Pages, Joaquim Salvi, Christophe Collewet, and Josep Forest. Optimised De Bruijn Patterns for One-shot Shape Acquisition. *Image and Vision Computing*, 23(8):707–720, 2005. 2, 3, 4, 5
- [45] Jeffrey L Posdamer and Martin D Altschuler. Surface Measurement by Space-encoded Projected Beam Systems. *Computer Graphics and Image Processing*, 18(1):1–17, 1982. 2
- [46] Ryusuke Sagawa, Yuichi Ota, Yasushi Yagi, Ryo Furukawa, Naoki Asada, and Hiroshi Kawasaki. Dense 3D Reconstruction Method Using a Single Pattern for Fast Moving Object. In *ICCV*, pages 1779–1786. IEEE, 2009. 2
- [47] Ryusuke Sagawa, Hiroshi Kawasaki, Shota Kiyota, and Ryo Furukawa. Dense One-shot 3D Reconstruction by Detecting Continuous Regions with Parallel Line Projection. In *ICCV*, pages 1911–1918. IEEE, 2011. 2
- [48] Joaquim Salvi, Sergio Fernandez, Tomislav Pribanic, and Xavier Llado. A state of the art in structured light patterns for surface profilometry. *PR*, 43(8):2666–2680, 2010. 2
- [49] Jianwen Song, Kai Liu, Arcot Sowmya, and Changming Sun. Super-Resolution Phase Retrieval Network for Single-Pattern Structured Light 3D Imaging. *IEEE TIP*, 32:537–549, 2022. 2
- [50] V Srinivasan, Hsin-Chu Liu, and Maurice Halioua. Automated phase-measuring profilometry: a phase mapping approach. *Applied Optics*, 24(2):185–188, 1985. 2
- [51] Xianyu Su and Qican Zhang. Dynamic 3-D shape measurement method: A review. *Optics and Lasers in Engineering*, 48(2):191–204, 2010. 2
- [52] Johji Tajima and Masato Iwakawa. 3-D data acquisition by Rainbow Range Finder. In *ICPR*, pages 309–313. IEEE, 1990. 2
- [53] Mitsuo Takeda and Kazuhiro Mutoh. Fourier Transform Profilometry for the Automatic Measurement of 3-D Object Shapes. *Applied Optics*, 22(24):3977–3982, 1983. 2
- [54] Borom Tunwattanapong, Graham Fyffe, Paul Graham, Jay Busch, Xueming Yu, Abhijeet Ghosh, and Paul Debevec. Acquiring Reflectance and Shape from Continuous Spherical Harmonic Illumination. *ACM TOG*, 32(4):1–12, 2013. 2
- [55] Lawrence B. Wolff and Terrance E. Boult. Constraining Object Features Using a Polarization Reflectance Model. *IEEE TPAMI*, 13(7):635–657, 1991. 7
- [56] Xianmin Xu, Yuxin Lin, Haoyang Zhou, Chong Zeng, Yaxin Yu, Kun Zhou, and Hongzhi Wu. A unified spatial-angular structured light for single-view acquisition of shape and reflectance. In *CVPR*, pages 206–215, 2023. 1, 2, 3
- [57] Kohei Yamashita, Yuto Enyo, Shohei Nobuhara, and Ko Nishino. nLMVS-Net: Deep Non-Lambertian Multi-View Stereo. In *WACV*, pages 3037–3046, 2023. 1, 2
- [58] Lili Yang, Fu Li, Zhiwei Xiong, Guangming Shi, Yi Niu, and Ruodai Li. Single-shot Dense Depth Sensing with Frequency-division Multiplexing Fringe Projection. *Journal of Visual Communication and Image Representation*, 46:139–149, 2017. 2
- [59] Ye Yu and William AP Smith. InverseRenderNet: Learning Single Image Inverse Rendering. In *CVPR*, pages 3155–3164, 2019. 1, 2
- [60] Kai Zhang, Fujun Luan, Qianqian Wang, Kavita Bala, and Noah Snavely. Physg: Inverse rendering with spherical gaussians for physics-based material editing and relighting. In *CVPR*, pages 5453–5462, 2021. 1, 2
- [61] Li Zhang, Brian Curless, and Steven M Seitz. Rapid Shape Acquisition Using Color Structured Light and Multi-pass Dynamic Programming. In *3DPVT*, pages 24–36. IEEE, 2002. 2, 3, 4, 5, 6
- [62] Xiao Zhou, Cong Zhou, Yu Kang, Tingting Zhang, and Xingang Mou. Pattern Encoding of Robust M-Array Driven by Texture Constraints. *IEEE Transactions on Instrumentation and Measurement*, 72:1–16, 2023. 2
- [63] Zhenglong Zhou, Zhe Wu, and Ping Tan. Multi-view Photometric Stereo with Spatially Varying Isotropic Materials. In *CVPR*, pages 1482–1489, 2013. 2

Spatial Polarization Multiplexing: Single-Shot Invisible Shape and Reflectance Recovery

Supplementary Material

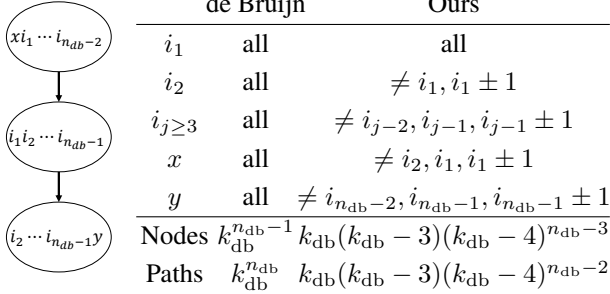


Figure A.1. The diagram of the graph that generates the de Bruijn sequence. Each node represents a substring of $n_{db} - 1$ length. Each path represents the transition of the substrings of n_{db} length. The right table shows the possible symbols for each position. We impose constraints on the de Bruijn sequence to prevent adjacent stripes with close AoLP values.

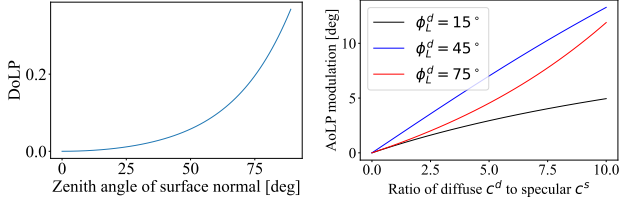


Figure A.2. **Left:** DoLP of diffuse reflection modeled as Fresnel transmission for the zenith angle of the surface normal. The DoLP is much lower than 1.0 for most zenith angles. **Right:** AoLP modulation for $\frac{c^d}{c^s}$. Even when diffuse reflection is dominant, modulation of incident AoLP is within only a few degrees.

A.1. Polarization Projector

A polarization projector can control the polarization orientation at each pixel instead of the light intensity [24, 32]. The key component of the polarization projector is a Spatial Light Modulator (SLM) made of a Twisted Nematic (TN) liquid crystal. The liquid crystal shows both fluidity and anisotropy, which allows us to change its anisotropy with external force. The TN liquid crystal has perpendicularly aligned elongated molecules on each side, resulting in helically oriented molecules through its inside. Such helical structure guides and changes the polarization orientation of incident light. By applying the voltage between both sides of the liquid crystal, we can disturb its helical structure and weaken its guidance of polarization orientation, which enables us to control the rotation of polarization.

The SLM has a two-dimensional array of TN liquid crystals placed between electrodes. By controlling the voltage

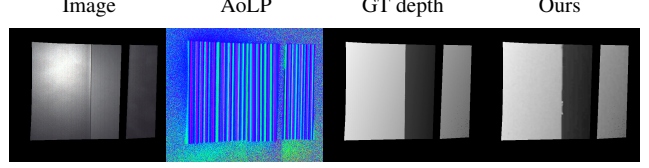


Figure A.3. Depth reconstruction results of scenes with occlusion. Our method can accurately handle occlusion.

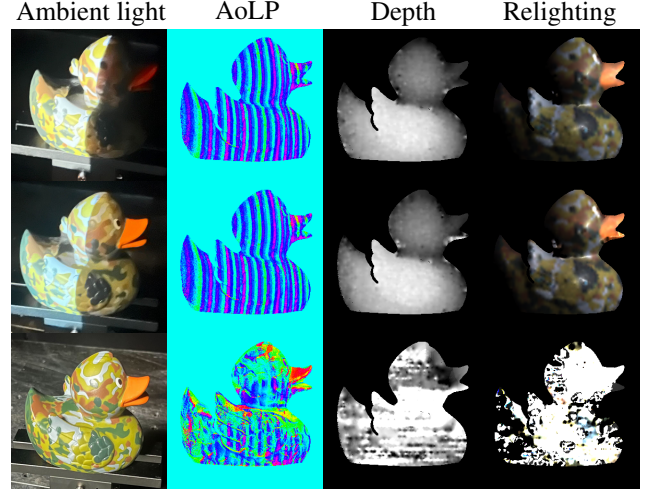


Figure A.4. Observed AoLP and reconstruction results under different ambient light. The leftmost image is a reference image to show the intensity of ambient light compared with the projector light projected onto the left side of the object.

between the electrodes of each cell, we can rotate the polarization orientation of incident polarized light at each pixel independently and project the polarization pattern. Since the range of AoLP rotation is from 0° to 90° continuously, we can realize complex polarization patterns with the polarization projector.

A.2. Constrained de Bruijn Sequence

The original de Bruijn sequence is generated as the Eulerian path of the oriented graph whose nodes represent all possible strings of length $n_{db} - 1$ and edges represent the substrings of length n_{db} [15]. In this graph, each edge connects two nodes whose strings partially overlap to represent a substring of length n_{db} . Since we can concatenate one of k_{db} symbols to the front or back of each node to make substrings, the in-degree and out-degree of each node are k_{db} , which indicates this graph has an Eulerian path.

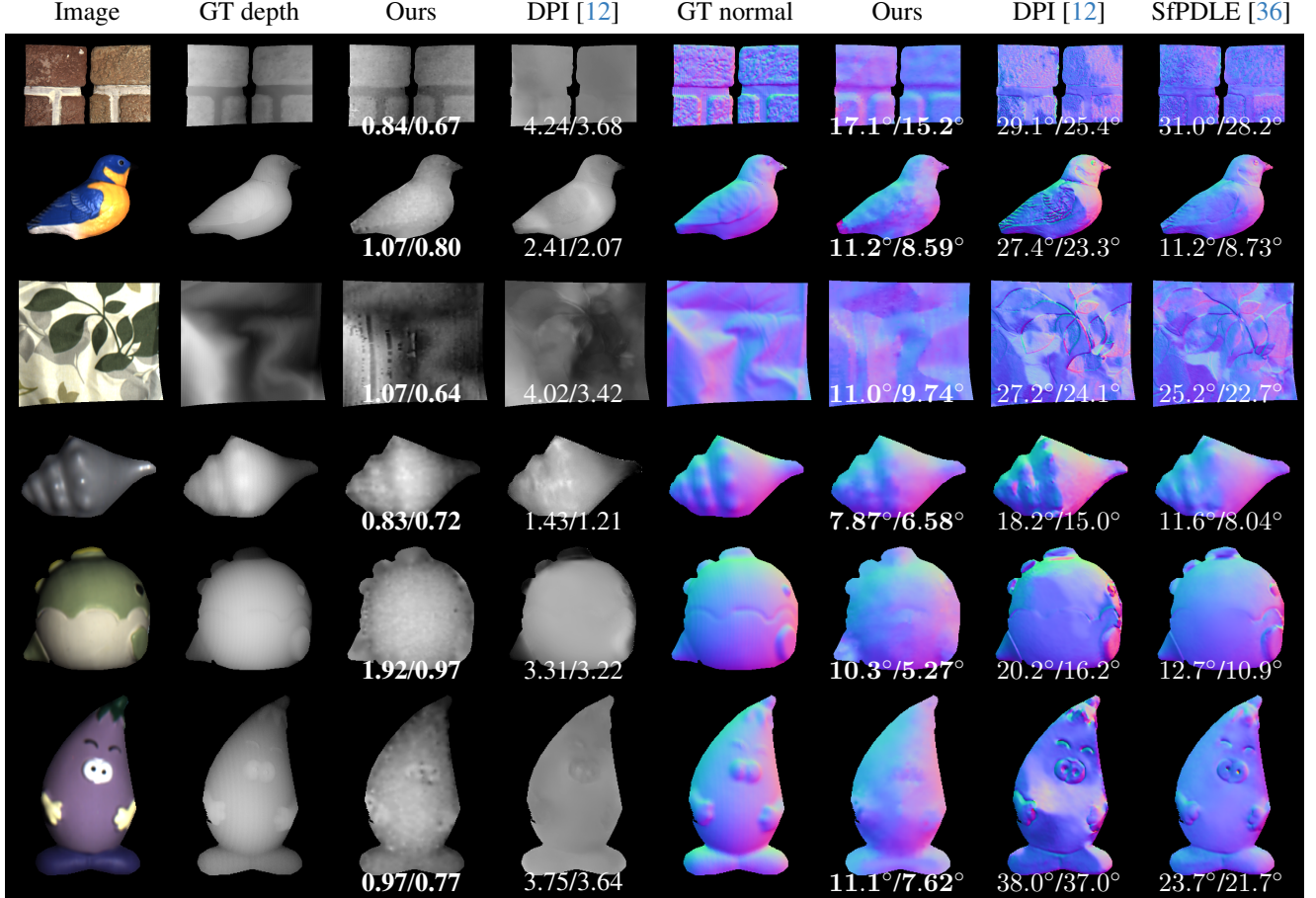


Figure A.5. Additional shape reconstruction results. The numbers below each map indicate the mean and median of depth errors in millimeters and angular errors in degrees.

As mentioned in the main paper, we impose two constraints for the de Bruijn sequence. First, AoLP values of three sequential elements must be different for polarimetric decomposition. Second, the differences between AoLP values of adjacent elements must be more than one quantization step for robust stripe detection. By denoting k_{db} symbols as $0, 1, \dots, k_{\text{db}} - 1$ and monotonically assigning each quantized AoLP value to the symbols, our two constraints on the de Bruijn sequence become $p_j \neq p_{j-2}, p_{j-1}, p_{j-1} \pm 1$ for all j , where p_j is the symbol of the j -th element.

As shown in Fig. A.1, we modify the oriented graph by removing the nodes and edges representing the substrings that violate our constraints. When $n_{\text{db}} \geq 3$ and $k_{\text{db}} \geq 5$, we can concatenate one of the $k_{\text{db}} - 4$ symbols to the front or back of each remaining node. Since the in-degree and out-degree of each node are $k_{\text{db}} - 4$ in the modified graph, it has an Eulerian path. The graph has $k_{\text{db}}(k_{\text{db}} - 3)(k_{\text{db}} - 4)^{n_{\text{db}} - 3}$ nodes. The number of length-

n_{db} substrings in the generated sequence is equal to the number of edges, $k_{\text{db}}(k_{\text{db}} - 3)(k_{\text{db}} - 4)^{n_{\text{db}} - 2}$. We find the Eulerian path of the modified graph by Hierholzer’s algorithm to generate the constrained de Bruijn sequence. Our polarization pattern is constructed by assigning quantized AoLP values to the generated sequence of symbols.

A.3. AoLP Modulation by Diffuse Reflection

Polarization of diffuse reflection is modeled with Fresnel transmission on the surface [2, 23]. In the left graph of Fig. A.2, we plot the DoLP of diffuse reflection modeled as Fresnel transmission [2, 23] for the zenith angle of the surface normal when the refractive index is 1.5. The diffuse DoLP ρ_L^d is much lower than 1.0 for all zenith angles. In particular, when the zenith angle is less than 45° , the diffuse DoLP is $\rho_L^d < 0.05$.

In the right graph of Fig. A.2, we show the AoLP modulation for $\frac{e^d}{c^s}$ when $\frac{\rho_L^d}{\rho_L^i} = 0.05$ and $\phi_L^i = 0$. Even when

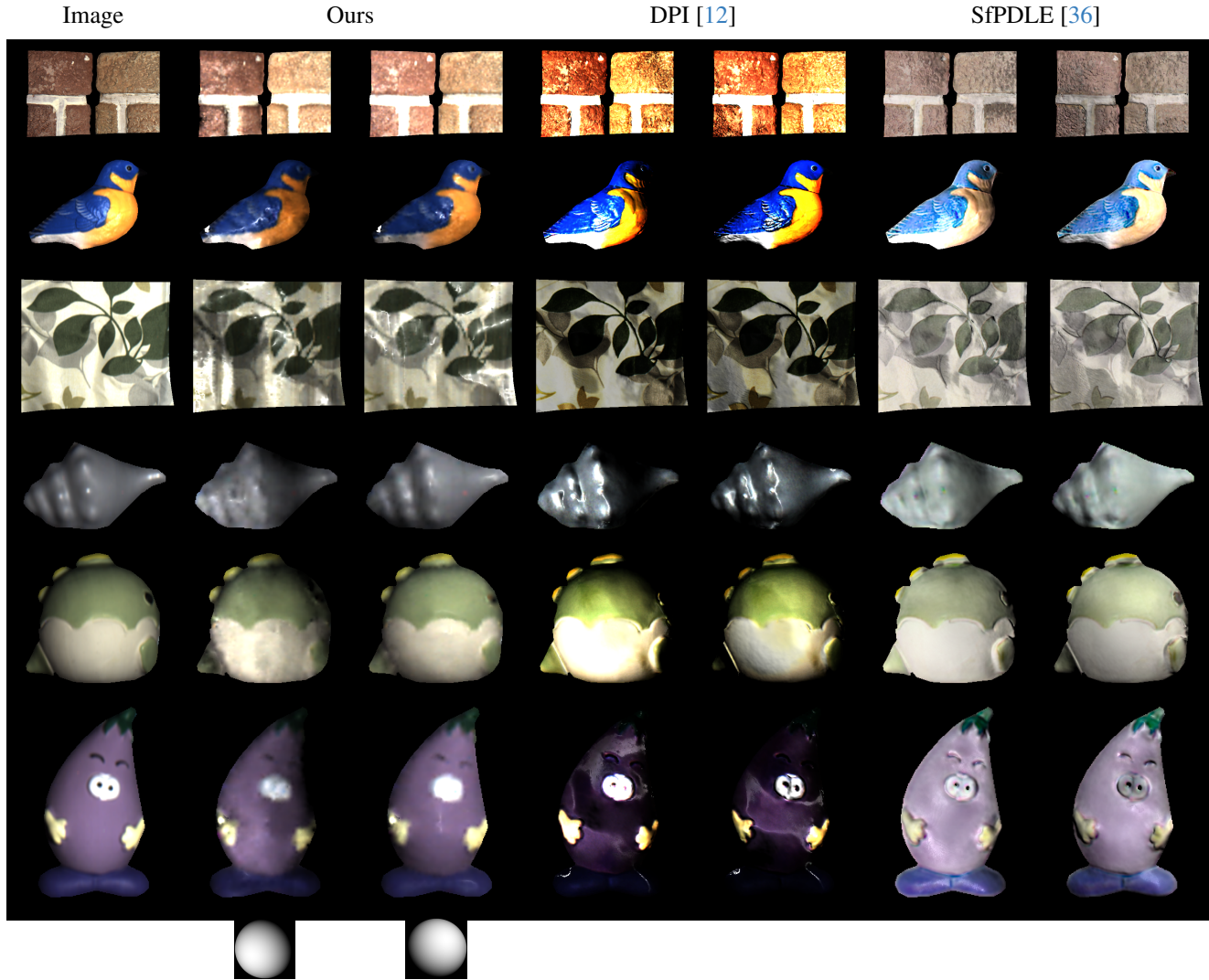


Figure A.6. Additional relighting results. The Lambertian sphere at the bottom of the figure indicates the direction of light.

the diffuse reflection c^d is dominant, the AoLP modulation is within only a few degrees.

A.4. Shape Reconstruction with Occlusion

Figure A.3 shows shape reconstruction results of scenes with occlusion. Decoding by dynamic programming can successfully handle the occlusion. Occlusions for the camera are omitted as not-detected symbols during dynamic programming. Occlusions for the projector are not detected as symbols or they are corrected as misdetections.

A.5. Additional Experimental Results

Figures A.5 and A.6 show additional experimental results of shape reconstruction and relighting on various objects of

different shapes and materials. Our method can accurately reconstruct both shape and reflectance from a single polarimetric image, compared with learning-based methods.

A.6. Limitation

Figure A.4 experimentally shows the effect of ambient light on our method. While we can reconstruct shape and reflectance under weak ambient light, strong ambient light compared with projector light affects the observed AoLP image, leading to failures in decoding. A naive approach to handling ambient light is to use a more powerful light source. Another approach is to exploit the modulated AoLP pattern. Even when the ambient light is stronger than the projector light, a stripe AoLP pattern remains in the AoLP image. Using this modulated polarization pattern as the

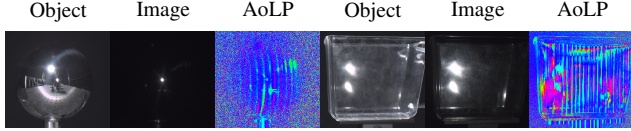


Figure A.7. Highly specular and transparent materials can be challenging for SPM reconstruction. The reflected polarization pattern is too noisy in the large regions.

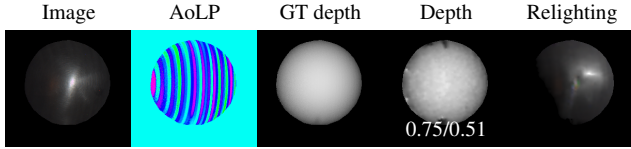


Figure A.8. Reconstruction results of a metallic surface. The reconstructed reflectance cannot represent photometric properties on a metallic surface different from a dielectric surface, such as color shift [11].

guide for inverse rendering under natural illumination is one of our future directions.

Even though quantization makes detection of the projected AoLP robust to the AoLP modulation by diffuse reflection, there are two cases where the correct decoding is difficult. The first case is when the object surface shows very narrow specular highlights. In this case, $c^s = 0$ on most of the surface regions and the reflected AoLP is largely modulated. The second case is when the zenith angle of the surface normal is close to the grazing angle, which causes large diffuse DoLP ρ_L^d .

Our method does not consider inter-reflection on the object surface. Inter-reflection disturbs the encoded polarization state of direct reflection. An object with a complex shape may cause errors in decoding and reflectance recovery due to inter-reflection.

Similar to many structured light methods, highly specular surfaces and transparent objects cause challenges. As shown in Fig. A.7, the reflected light on a highly specular surface is observed only in a small region with a specific surface normal, which prevents us from observing the reflected polarization pattern. Transparent surface shows a distorted polarization pattern due to transmitted light after inter-reflection within the object.

Since the FMRDF model [23] assumes a dielectric surface, our BRDF reconstruction method is limited to such materials. Figure A.8 shows shape reconstruction and relighting results of a rough metallic surface. Since the AoLP pattern is retained before and after reflection, our method can decode this pattern correctly and reconstruct the object shape. Although relighting results capture the surface roughness, the reconstructed reflectance cannot correctly represent color shift on the metallic surface [11]. The metallic surface also shows a different polarimetric behavior from

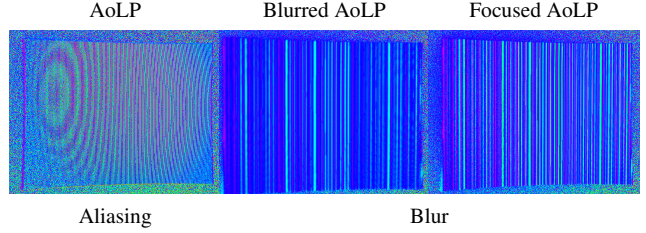


Figure A.9. The limitation of reconstruction resolution. Narrow stripe width causes aliasing and is susceptible to blur of the polarization projector.

a dielectric surface. Phase delay on the metallic surface causes circular polarization [3]. Combining a polarimetric reflectance model of a conductor [29] with our SPM to analyze these radiometric and polarimetric behaviors will allow for reflectance recovery of metallic surfaces in the future.

The resolution of single-shot reconstruction is limited by two factors. First, aliasing occurs between the polarization pattern and a sensor array of a polarimetric camera. To capture the correct polarization states, a set of pixels on the polarimetric camera with four on-chip polarization filters needs to observe the same polarization states. Second, the blur of the polarization projector changes incident polarization states at the edge of the stripe pattern. If the stripe width is narrower than the blur, the AoLP values of each line may be modulated. Figure A.9 shows the effect of aliasing and blur. To avoid these effects, the stripe width must be sufficiently wide. We empirically set 12 pixels as the width of the stripe for our current hardware. This limited resolution of reconstruction loses a detailed surface texture. Advances in hardware (*e.g.*, liquid crystal spatial light modulator) will increase the reconstruction resolution and mitigate this problem.